Discovery of a Shock-compressed Magnetic Field in the Northwestern Rim of the Young Supernova Remnant RX J1713.7–3946 with X-Ray Polarimetry

Riccardo Ferrazzoli, Dmitry Prokhorov, Niccolò Bucciantini, Patrick Slane, Jacco Vink, Martina Cardillo, Yi-Jung Yang, Stefano Silvestri, Ping Zhou, Enrico Costa, et al.

The Astrophysical Journal Letters, 967:L38 (15pp), 2024 June 1 https://doi.org/10.3847/2041-8213/ad4a68

Discovery of a Shock-compressed Magnetic Field in the Northwestern Rim of the Young Supernova Remnant RX J1713.7–3946 with X-Ray Polarimetry

Riccardo Ferrazzoli[1], Dmitry Prokhorov[2,3], Niccolò Bucciantini[4,5,6], Patrick Slane[7], Jacco Vink[3], Martina Cardillo[1], Yi-Jung Yang[8,9,10,11], Stefano Silvestri[12], Ping Zhou[13], Enrico Costa[1], Nicola Omodei[14], C.-Y. Ng[15], Paolo Soffitta[1], Martin C. Weisskopf[16], Luca Baldini[12,17], Alessandro Di Marco[1], Victor Doroshenko[18], Jeremy Heyl[19], Philip Kaaret[16], Dawoon E. Kim[1,20,21], Frédéric Marin[22], Tsunefumi Mizuno[23], Melissa Pesce-Rollins[12], Carmelo Sgrò[12], Douglas A. Swartz[24], Toru Tamagawa[25], Fei Xie[1,26], Iván Agudo[27], Lucio A. Antonelli[28,29], Matteo Bachetti[30], Wayne H. Baumgartner[16], Ronaldo Bellazzini[12], Stefano Bianchi[31], Stephen D. Bongiorno[16], Raffaella Bonino[32,33], Alessandro Brez[12], Fiamma Capitanio[1], Simone Castellano[12], Elisabetta Cavazzuti[34], Chien-Ting Chen[24], Stefano Ciprini[29,35], Alessandra De Rosa[1], Ettore Del Monte[1], Laura Di Gesu[34], Niccolò Di Lalla[14], Immacolata Donnarumma[34], Michal Dovčiak[36], Steven R. Ehlert[16], Teruaki Enoto[25], Yuri Evangelista[1], Sergio Fabiani[1], Javier A. Garcia[37], Shuichi Gunji[38], Kiyoshi Hayashida[39], Wataru Iwakiri[40], Svetlana G. Jorstad[41,42], Vladimir Karas[36], Fabian Kislat[43], Takao Kitaguchi[25], Jeffery J. Kolodziejczak[16], Henric Krawczynski[44], Fabio La Monaca[1,20,21], Luca Latronico[32], Ioannis Liodakis[16], Simone Maldera[32], Alberto Manfreda[45], Andrea Marinucci[34], Alan P. Marscher[41], Herman L. Marshall[46], Francesco Massaro[32,33], Giorgio Matt[31], Ikuyuki Mitsuishi[47], Fabio Muleri[1], Michela Negro[48], Stephen L. O'Dell[16], Chiara Oppedisano[32], Alessandro Papitto[28], George G. Pavlov[49], Abel L. Peirson[14], Matteo Perri[28,29], Pierre-Olivier Petrucci[50], Maura Pilia[30], Andrea Possenti[30], Juri Poutanen[51], Simonetta Puccetti[29], Brian D. Ramsey[16], John Rankin[1], Ajay Ratheesh[1], Oliver J. Roberts[24], Roger W. Romani[14], Gloria Spandre[12], Fabrizio Tavecchio[52], Roberto Taverna[53], Yuzuru Tawara[47], Allyn F. Tennant[16], Nicholas E. Thomas[16], Francesco Tombesi[20,35,54], Alessio Trois[30], Sergey S. Tsygankov[51], Roberto Turolla[53,55], Kinwah Wu[55], and Silvia Zane[55]

[1] INAF Istituto di Astrofisica e Planetologia Spaziali, Via del Fosso del Cavaliere 100, 00133 Roma, Italy; riccardo.ferrazzoli@inaf.it
[2] Institute of Physics of Academia Sinica, No. 128, Section 2, Academia Road, Nangang District, Taipei City, Taiwan
[3] Anton Pannekoek Institute for Astronomy & GRAPPA, University of Amsterdam, Science Park 904, 1098 XH Amsterdam, The Netherlands
[4] INAF Osservatorio Astrofisico di Arcetri, Largo Enrico Fermi 5, 50125 Firenze, Italy
[5] Dipartimento di Fisica e Astronomia, Università degli Studi di Firenze, Via Sansone 1, 50019 Sesto Fiorentino (FI), Italy
[6] Istituto Nazionale di Fisica Nucleare, Sezione di Firenze, Via Sansone 1, 50019 Sesto Fiorentino (FI), Italy
[7] Center for Astrophysics | Harvard & Smithsonian, 60 Garden Street, Cambridge, MA 02138, USA
[8] Department of Physics, The University of Hong Kong, Pokfulam Road, Hong Kong
[9] Laboratory for Space Research, The University of Hong Kong, Cyberport 4, Hong Kong
[10] Department of Physics, National Cheng Kung University, University Road, Tainan, Taiwan
[11] Graduate Institute of Astronomy, National Central University, 300 Zhongda Road, Zhongli, Taoyuan 32001, Taiwan
[12] Istituto Nazionale di Fisica Nucleare, Sezione di Pisa, Largo B. Pontecorvo 3, 56127 Pisa, Italy
[13] School of Astronomy and Space Science, Nanjing University, Nanjing 210023, People's Republic of China
[14] Department of Physics and Kavli Institute for Particle Astrophysics and Cosmology, Stanford University, Stanford, CA 94305, USA
[15] Department of Physics, The University of Hong Kong, Pokfulam, Hong Kong
[16] NASA Marshall Space Flight Center, Huntsville, AL 35812, USA
[17] Dipartimento di Fisica, Università di Pisa, Largo B. Pontecorvo 3, 56127 Pisa, Italy
[18] Institut für Astronomie und Astrophysik, Universität Tübingen, Sand 1, 72076 Tübingen, Germany
[19] University of British Columbia, Vancouver, BC V6T 1Z4, Canada
[20] Dipartimento di Fisica, Università degli Studi di Roma "Tor Vergata", Via della Ricerca Scientifica 1, 00133 Roma, Italy
[21] Dipartimento di Fisica, Università degli Studi di Roma "La Sapienza", Piazzale Aldo Moro 5, 00185 Roma, Italy
[22] Université de Strasbourg, CNRS, Observatoire Astronomique de Strasbourg, UMR 7550, 67000 Strasbourg, France
[23] Hiroshima Astrophysical Science Center, Hiroshima University, 1-3-1 Kagamiyama, Higashi-Hiroshima, Hiroshima 739-8526, Japan
[24] Science and Technology Institute, Universities Space Research Association, Huntsville, AL 35805, USA
[25] RIKEN Cluster for Pioneering Research, 2-1 Hirosawa, Wako, Saitama 351-0198, Japan
[26] Guangxi Key Laboratory for Relativistic Astrophysics, School of Physical Science and Technology, Guangxi University, Nanning 530004, People's Republic of China
[27] Instituto de Astrofísica de Andalucía–CSIC, Glorieta de la Astronomía s/n, 18008 Granada, Spain
[28] INAF Osservatorio Astronomico di Roma, Via Frascati 33, 00078 Monte Porzio Catone (RM), Italy
[29] Space Science Data Center, Agenzia Spaziale Italiana, Via del Politecnico snc, 00133 Roma, Italy
[30] INAF Osservatorio Astronomico di Cagliari, Via della Scienza 5, 09047 Selargius (CA), Italy
[31] Dipartimento di Matematica e Fisica, Università degli Studi Roma Tre, Via della Vasca Navale 84, 00146 Roma, Italy
[32] Istituto Nazionale di Fisica Nucleare, Sezione di Torino, Via Pietro Giuria 1, 10125 Torino, Italy
[33] Dipartimento di Fisica, Università degli Studi di Torino, Via Pietro Giuria 1, 10125 Torino, Italy
[34] ASI—Agenzia Spaziale Italiana, Via del Politecnico snc, 00133 Roma, Italy
[35] Istituto Nazionale di Fisica Nucleare, Sezione di Roma "Tor Vergata", Via della Ricerca Scientifica 1, 00133 Roma, Italy
[36] Astronomical Institute of the Czech Academy of Sciences, Boční II 1401/1, 14100 Praha 4, Czech Republic
[37] NASA Goddard Space Flight Center, Greenbelt, MD 20771, USA
[38] Yamagata University,1-4-12 Kojirakawa-machi, Yamagata-shi 990-8560, Japan
[39] Osaka University, 1-1 Yamadaoka, Suita, Osaka 565-0871, Japan
[40] International Center for Hadron Astrophysics, Chiba University, Chiba 263-8522, Japan
[41] Institute for Astrophysical Research, Boston University, 725 Commonwealth Avenue, Boston, MA 02215, USA
[42] Department of Astrophysics, St. Petersburg State University, Universitetsky pr. 28, Petrodvoretz, 198504 St. Petersburg, Russia

[43] Department of Physics and Astronomy and Space Science Center, University of New Hampshire, Durham, NH 03824, USA
[44] Physics Department and McDonnell Center for the Space Sciences, Washington University in St. Louis, St. Louis, MO 63130, USA
[45] Istituto Nazionale di Fisica Nucleare, Sezione di Napoli, Strada Comunale Cinthia, 80126 Napoli, Italy
[46] MIT Kavli Institute for Astrophysics and Space Research, Massachusetts Institute of Technology, 77 Massachusetts Avenue, Cambridge, MA 02139, USA
[47] Graduate School of Science, Division of Particle and Astrophysical Science, Nagoya University, Furo-cho, Chikusa-ku, Nagoya, Aichi 464-8602, Japan
[48] Department of Physics and Astronomy, Louisiana State University, Baton Rouge, LA 70803, USA
[49] Department of Astronomy and Astrophysics, Pennsylvania State University, University Park, PA 16802, USA
[50] Université Grenoble Alpes, CNRS, IPAG, 38000 Grenoble, France
[51] Department of Physics and Astronomy, 20014 University of Turku, Finland
[52] INAF Osservatorio Astronomico di Brera, Via E. Bianchi 46, 23807 Merate (LC), Italy
[53] Dipartimento di Fisica e Astronomia, Università degli Studi di Padova, Via Marzolo 8, 35131 Padova, Italy
[54] Department of Astronomy, University of Maryland, College Park, MD 20742, USA
[55] Mullard Space Science Laboratory, University College London, Holmbury St Mary, Dorking, Surrey RH5 6NT, UK
Received 2024 March 11; revised 2024 May 3; accepted 2024 May 11; published 2024 May 30

Abstract

Supernova remnants (SNRs) provide insights into cosmic-ray acceleration and magnetic field dynamics at shock fronts. Recent X-ray polarimetric measurements by the Imaging X-ray Polarimetry Explorer (IXPE) have revealed radial magnetic fields near particle acceleration sites in young SNRs, including Cassiopeia A, Tycho, and SN 1006. We present here the spatially resolved IXPE X-ray polarimetric observation of the northwestern rim of SNR RX J1713.7–3946. For the first time, our analysis shows that the magnetic field in the particle acceleration sites of this SNR is oriented tangentially with respect to the shock front. Because of the lack of precise Faraday rotation measurements in the radio band, this was not possible before. The average measured polarization degree (PD) of the synchrotron emission is $12.5\% \pm 3.3\%$, lower than the one measured by IXPE in SN 1006, comparable to the Tycho one, but notably higher than the one in Cassiopeia A. On subparsec scales, localized patches within RX J1713.7–3946 display a PD of up to $41.5\% \pm 9.5\%$. These results are compatible with a shock-compressed magnetic field. However, in order to explain the observed PD, either the presence of a radial net magnetic field upstream of the shock or partial reisotropization of the turbulence downstream by radial magnetohydrodynamical instabilities can be invoked. From comparison of PD and magnetic field distribution with γ-rays and ^{12}CO data, our results provide new inputs in favor of a leptonic origin of the γ-ray emission.

Unified Astronomy Thesaurus concepts: X-ray astronomy (1810); Polarimetry (1278); Supernova remnants (1667)

1. Introduction

Supernova remnants (SNRs) are thought to play an essential role in accelerating Galactic cosmic rays (CRs), with diffusive shock acceleration (DSA) generally accepted as the leading mechanism (see, e.g., Malkov & Drury 2001). This mechanism is capable of accelerating CRs up to hundreds of TeV energies (see, e.g., Ginzburg & Syrovatskii 1964; Amato 2014) thanks to an amplified magnetic field. Evidence of its presence in the SNR is provided by nonthermal X-ray emission generated by relativistic gyrating electrons, known as synchrotron radiation, first seen in radio waves (see, e.g., van der Laan 1962), and then in the X-ray band (Koyama et al. 1995). The discovery of X-ray synchrotron emission in SNRs provided crucial information on the acceleration of electrons up to TeV energies. However, the exact relationship between magnetic fields influencing CR acceleration and CRs modifying magnetic fields is still an open question. Indeed, the presence of synchrotron alone cannot be considered a definitive proof of CR presence. CRs are mainly protons and, in order to be sure that a source is accelerating protons, detection of hadronic γ-ray emission due to neutral pion decay is needed (Ackermann et al. 2013; Amato 2014; Cristofari 2021).

Polarimetry provides information on the magnetic field turbulence level, and indeed, radio-band polarimetry revealed that young (up to a few thousand yr old) SNRs show low polarization fractions of 5%−10% (e.g., Dickel & Jones 1990), indicative of high turbulence, and a preferential radial direction of the magnetic field. On the other hand, older (∼10,000 yr old or more) SNRs show a more ordered and preferentially tangential magnetic field orientation (Milne & Dickel 1975; Fürst & Reich 2004). While the latter can be easily interpreted as shock compression of the ambient magnetic field, which enhances the tangential component, the radial magnetic field orientation is less understood, with most theories invoking radial stretching induced by the onset of hydrodynamical instabilities, such as Rayleigh–Taylor (RT) at the SNR contact discontinuity (CD; Gull 1973; Jun & Norman 1996) or Richtmeyer–Meshkov (RM) instabilities near the forward shock (Inoue et al. 2013). As an alternative, the radial magnetic field orientation may appear as an artifact of preferential (i.e., more efficient) electron acceleration, where the magnetic field is parallel to the shock normal, biasing polarization measurements toward regions with a radial magnetic field direction (West et al. 2017).

Once relegated only to the radio and, in some cases, in the infrared band (e.g., Jones et al. 2003), the polarimetric study of the magnetic field topology in young SNRs can now also be explored in X-rays thanks to the launch of the NASA/ASI Imaging X-ray Polarimetric Explorer (IXPE; Weisskopf et al. 2022), whose imaging capabilities are perfectly suited for probing magnetic field distribution and turbulence in high-energy extended sources, such as SNRs. X-ray-band polarimetry has many advantages with respect to that in the radio band: TeV-energy electrons responsible for the X-ray emission have a shorter lifetime compared to the radio-emitting electrons (Vink & Zhou 2018). For this reason, they are confined in regions closer to particle acceleration sites. Moreover, in the

X-ray band, the synchrotron spectra of SNRs tend to be steeper than in the radio one, and because the synchrotron polarization degree (PD) depends on the photon spectral index (Ginzburg & Syrovatskii 1965), this allows for higher theoretical maximum polarization values. Finally, X-ray radiation is not affected by Faraday rotation. Consequently, X-ray polarimetry provides the perfect opportunity to investigate magnetic field geometry at particle acceleration sites.

IXPE previously detected significant polarization in three younger SNRs: Cas A (Vink et al. 2022), Tycho (Ferrazzoli et al. 2023), and SN 1006 (Zhou et al. 2023), all showing radially oriented magnetic fields. This demonstrates that the processes responsible for radial magnetic fields observed in young SNRs are already at work at the scales where X-rays are emitted. The lowest PD of the nonthermal emission was reported for Cas A (Vink et al. 2022), PD $\sim$ 5%, followed by Tycho (Ferrazzoli et al. 2023), PD $\sim$ 12%, and finally by SN 1006 (Zhou et al. 2023), PD $\sim$ 22%. Comparing the X-ray polarization measurements of these three remnants, the remarkable similarity in the radially oriented magnetic field is in contrast with the very different PD, likely reflecting a decreasing level of magnetic field turbulence. The influence of different environmental densities has been put forward as a possible explanation (Zhou et al. 2023).

Here, we present a significant IXPE detection of a tangential magnetic field in the northwestern rim of the SNR RX J1713.7–3946 (from now on RX J1713 for brevity).

Also known as G347.3–0.5, RX J1713 is a very large ($\approx$1° diameter) shell-type SNR residing in the Galactic plane, discovered in the ROSAT all-sky survey (Pfeffermann & Aschenbach 1996). Its distance, inferred from CO observations and from investigation of X-ray-absorbing material in the remnant, is $\sim$1 kpc (Fukui et al. 2003; Uchiyama et al. 2003; Cassam-Chenaï et al. 2004). This remnant is thought to be the result of a Type Ib/c supernova explosion (also referred to as a "stripped core-collapse supernova") of a relatively low-mass star in a close binary system (Katsuda et al. 2015), where the progenitor massive hydrogen envelope was removed either in a binary interaction or through a stellar wind. RX J1713 is commonly associated with SN 393 (Wang et al. 1997; Tsuji & Uchiyama 2016; Acero et al. 2017), making it the oldest remnant for which an X-ray polarization signal is reported so far, with an age of 1631 yr.

Its hard X-ray emission has been discovered to be purely nonthermal (Koyama et al. 1997; Slane et al. 1999), representing the second detection of synchrotron X-ray radiation from an SNR shell after SN 1006. Lazendic et al. (2004) analyzed Chandra X-ray and Australia Telescope Compact Array (ATCA) 1.4 GHz radio observations of the northwestern region of RX J1713, resolving bright filaments of about 20″−40″ of inferred width, corresponding to linear sizes of 0.1−0.2 pc at a 1 kpc distance. Their analysis showed a one-to-one correspondence between X-ray and radio morphological structures, providing strong evidence that, in this part of the remnant, the same population of electrons is responsible for synchrotron emission in both the bands. Lazendic et al. (2004) also detected linear radio polarization from the SNR at the northwestern part of the shell, although Faraday rotation made it impossible to determine the magnetic field direction from the polarization vectors.

RX J1713 is also the best-studied young SNR in the γ-ray band: it has been detected at TeV energies by H.E.S.S. (Aharonian et al. 2004, 2007; H.E.S.S. Collaboration et al. 2018) and Fermi (Abdo et al. 2011; Federici et al. 2015). The finding was that the RX J1713 γ-ray emission at TeV energies closely follows the X-ray morphology. However, despite the detailed morphological and spectral studies, the nature of the mechanism responsible for the production of GeV and TeV γ-rays in RX J1713 has not clearly been established yet. There are different mechanisms that can be responsible for efficient γ-ray production: leptonic emission due to inverse-Compton scattering of soft—cosmic microwave background, IR, or optical—photons by relativistic electrons, hadronic emission due to two-photon decay of neutral pions produced by relativistic protons interacting with the ambient medium, or a mixture of both. RX J1713 is one of the most-debated sources in the discussion on γ-rays from the aforementioned radiation mechanisms. Acero et al. (2009) and H.E.S.S. Collaboration et al. (2018) argue that the γ-ray emission morphology, as well as the hardness of the spectrum, favors a leptonic origin, although it cannot be explained by a single electron population (Finke & Dermer 2012). Self-consistent hydrodynamical modeling, that includes the effects of efficient DSA, supports this interpretation (Ellison et al. 2010, 2012). The main argument there is that the density at the shock seems too low for a sufficiently high pion production rate from hadronic CRs. On the other hand, the hadronic mechanism could also fit data under the assumption that dense clumps have survived the shock passage. The most energetic hadronic CRs could penetrate those cloudlets, producing a relatively hard hadronic γ-ray spectrum (Fukui et al. 2012, 2021; Gabici & Aharonian 2014; Federici et al. 2015; Celli et al. 2019). A very recent hypothesis is that the emission could also be produced by the sum of reaccelerated CR electron emission and a subdominant contribution from freshly accelerated protons (Cristofari 2021). X-ray polarimetry is important, as it traces the level of magnetic field turbulence, which is one of the key ingredients of particle acceleration through DSA.

In this Letter, we describe the IXPE observation of RX J1713 and data reduction in Section 2; present and discuss our results in Sections 3 and 4, respectively; and finally, present our conclusions in Section 5.

2. Observation and Data Analysis

2.1. IXPE Data

As extensively outlined in Weisskopf et al. (2022) and its cited sources, the IXPE observatory is composed of three identical X-ray telescopes, each including an X-ray mirror module assembly (provided by NASA) and a polarization-sensitive gas pixel detector (GPD, provided by ASI; Costa et al. 2001; Bellazzini et al. 2006; Baldini et al. 2021; Soffitta et al. 2021). This configuration enables X-ray imaging spectro-polarimetry with $\sim$30″ angular resolution within the 2−8 keV energy band. IXPE observed the northwest part of the shell of RX J1713 (see Figure 1) three times in 2023: August 24–27, August 28–September 1, and September 24–October 5, for a total exposure time of $\sim$841 ks (ObsID 02001499). The pointing of the spacecraft was dithered with an amplitude of 0.′8 to further average out any residual instrumental effects. Because RX J1713 is among the faintest SNRs observed so far by IXPE, the background contribution needs to be carefully taken into account. This can be divided into two categories: the diffuse X-ray background of astrophysical origin and the

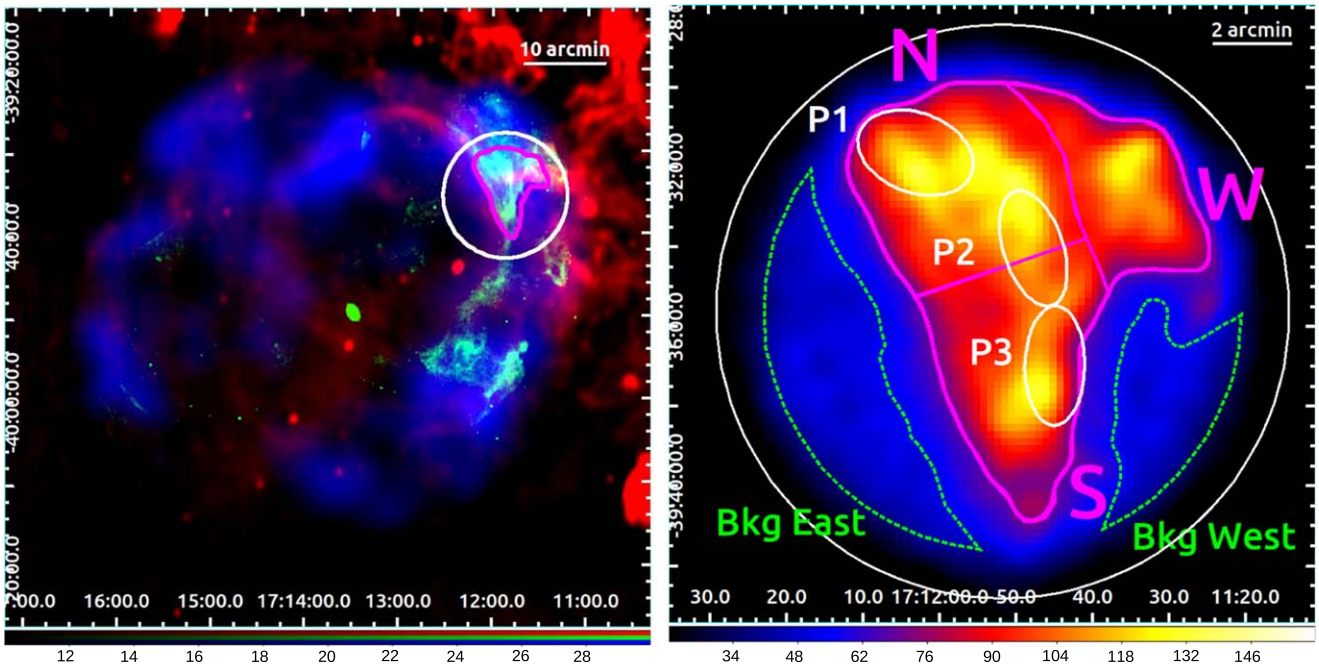

Figure 1. Left: three-color image of RX J1713: in red, the ATCA 20 cm image; in green, the 0.5−7 keV Chandra exposure-corrected mosaic; in blue, the H.E.S.S. >2 TeV excess count map. The magenta contour is the 2−5 keV IXPE emission, and the white circle is the IXPE field of view. Right: IXPE count map in the 2−5 keV band smoothed with a 30″ Gaussian kernel. In purple are marked the large-scale subregions of the shell selected for analysis: N, S, and W. The white ellipses are small-scale subregions also selected for analysis: P1, P2, and P3. The color bar represents the intensity per pixel. The background extraction regions are marked by dashed green lines.

particle-induced instrumental background. In order to mitigate the latter, we conducted an energy-dependent background rejection by removing the most probable particle-induced events through the algorithm of Di Marco et al. (2023). This allows one to remove up to 40% of the instrumental background events. After rejection, the 2−8 keV background level of previous IXPE observations is in the range $(0.9-1.2)\times10^{-3}$ counts s^{-1} $arcmin^{-2}$ (Di Marco et al. 2023). Because the remaining background after rejection is still nonnegligible, we select two source-free regions as seen in the right panel of Figure 1. In these regions, the emission consists of the remaining instrumental background, the Galactic ridge X-ray diffuse background, and the local sky background. The 2−8 keV total background counting rate from the two regions combined is found to be 2.2×10^{-3} counts s^{-1} $arcmin^{-2}$. We verified that the background is compatible with being unpolarized with PD < 7.5% in the 2−5 keV energy range and PD < 6.9% in the 2−8 keV energy range at a 99% confidence level. The details of the background properties are described in the Appendix.

A small fraction of the observation was affected by high solar activity, which caused background spikes in the data light curves. In order to remove the time intervals affected by this background contribution, we produced a light curve by binning the 2−8 keV photons from the whole data set every 15 s; we then fitted the histogram of the count distribution with a Gaussian function and filtered out all the time intervals with count rates more than 3σ above the mean of the distribution. Consequently, we removed ∼10 ks from the data, leaving an exposure time of ∼830 ks.

Because of uncertainties on the photon absorption point reconstruction in the GPD, spurious polarization patterns on scales comparable to the IXPE angular resolution may potentially contaminate Stokes maps in sources exhibiting significant gradients of the brightness distribution (that is, a second derivative). Through estimates based on a Mueller matrix characterization of the IXPE response (Bucciantini et al. 2023), we verified that the impact of this effect is negligible (≪1% polarization) in all the regions of interest considered in this work.

The alignment of the three detector units (DUs) was good, and no manual alignment was needed.

2.2. Data Analysis

Based on the well-tested procedure of previous IXPE analysis of SNRs (Vink et al. 2022; Ferrazzoli et al. 2023; Zhou et al. 2023), we adopt an approach that starts from a small-scale search of signal in binned and smoothed polarization maps and then goes on with a large-scale search in regions of interest using both model-independent and model-dependent analysis techniques. In this Letter, we produce polarization maps and perform model-independent analysis of IXPE data with the publicly available software package `ixpeobssim` (version 30.6.3; Baldini et al. 2022), using version 12 of the instrument response functions. `ixpeobssim` is a simulation and analysis toolkit developed by the IXPE collaboration including both a tool for generating realistic Monte Carlo simulations of IXPE observations and methods for data selection and binning to produce Stokes maps and spectra.

We used the algorithm `PMAPCUBE` of the `ixpeobssim` binning tool `xpbin` to produce images of the Stokes parameters I, Q, and U and then to compute PD and polarization angle (PA) maps.

We selected the 2−5 keV energy band to minimize the contamination from both instrumental and diffuse background (see Figure 7 in the Appendix).

For in-depth analysis, we chose a region delimited by the contour enclosing the shell with a surface brightness of at least

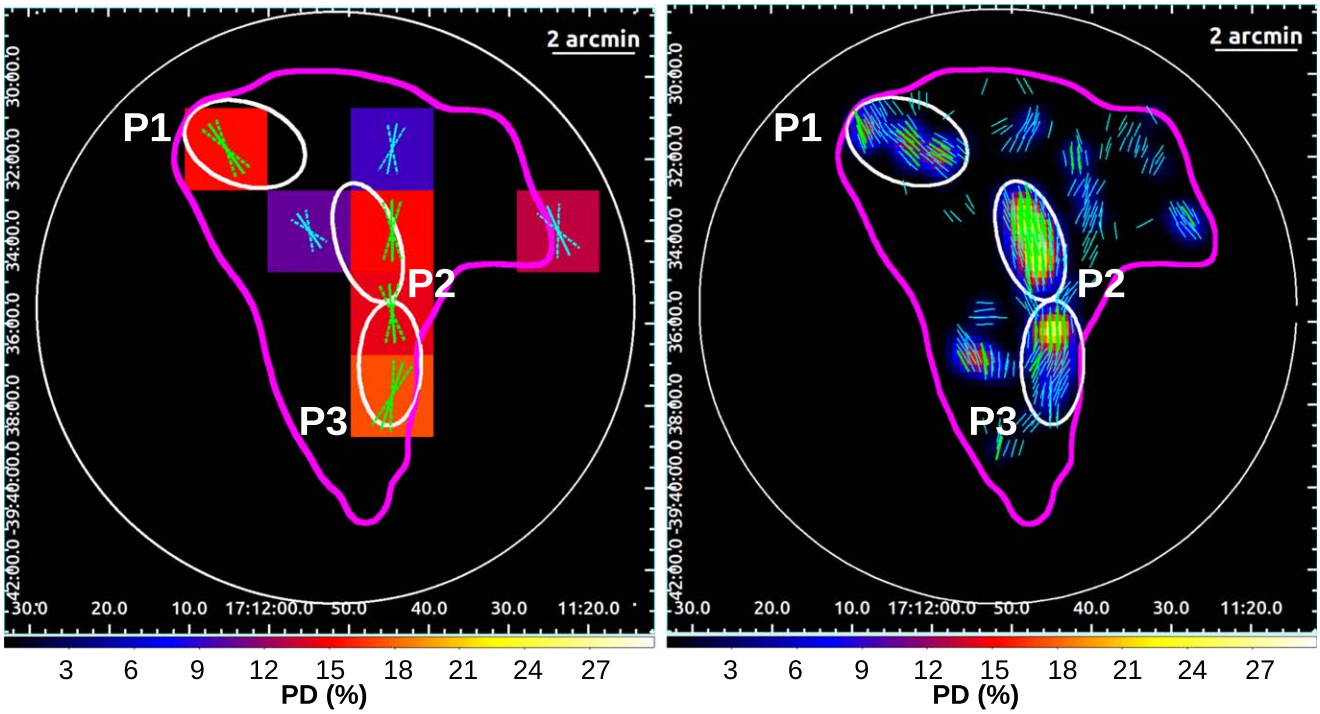

Figure 2. Left: polarization map binned with 2′ wide pixels. The cyan and green vectors represent the direction of the magnetic field revealed at 2σ and 3σ significance levels, respectively. The length of the vectors is proportional to the PD. The dashed vectors show the 2σ uncertainty on the magnetic field direction in each pixel to improve the visibility. Right: smoothed polarization map with a 1′ Gaussian kernel. As in the previous panel, the cyan and green vectors represent the direction of the magnetic field revealed at 2σ and 3σ significance levels, respectively. In both panels, we show the IXPE field of view as a white circle and the P1, P2, and P3 regions as white ellipses, while the 2−5 keV IXPE contours are in magenta and the color bar is the PD in percent.

0.90 counts arcsec^{-2} in the 2−5 keV energy range, that is, twice the background surface brightness of ∼0.45 counts arcsec^{-2}. We further divided the selected region into the north (N), south (S), and west (W) subregions and defined three elliptical subregions called P1, P2, and P3, identified in the smoothed polarization maps (see right panel of Figure 2). The large-scale search for polarization in the regions of interest was carried out with the `PCUBE` algorithm of the `xpbin` tool: this allows us to extract the Stokes parameters of the events collected in each region and to calculate polarization properties.

We also extracted the Stokes I, Q, and U spectra of these regions through the `PHA1`, `PHA1Q`, and `PHA1U` algorithms in `xpbin` in order to perform a model-dependent analysis using `XSPEC` version 12.12.1 (Arnaud 1996). In the spectropolarimetric analysis, we used weighted analysis and response files (Di Marco et al. 2022) that allow one to improve the detection sensitivity by weighting the photoelectron tracks through their elongation. We grouped the Stokes I spectra to contain at least 50 counts bin^{-1}, while we applied a constant 0.2 keV energy binning to the Stokes Q and U spectra.

2.3. Other Data

RX J1713 is a very well-studied object from radio to γ-ray energy bands. In Figure 1 (left), we show a composite three-color image of the whole RX J1713 in the radio (red; ATCA 20 cm), X-ray (green; Chandra 0.5−7 keV), and γ-ray (blue; H.E.S.S. >2 TeV) bands: the IXPE field of view covers a region that is bright in all three wavelengths.

Consequently, it is important to present the X-ray polarimetric results in a multiwavelength context. For this purpose, we use in our analysis several collected data sets.

For the radio band, we obtain data from ATCA, namely, the image and polarization fraction map at 20 cm (Lazendic et al. 2004). We also employed high-resolution X-ray data as an exposure-corrected Chandra broadband (0.5−7 keV) image obtained from a mosaic of ObsIDs 736, 737, 5560, 5561, 6370, 10090, 10091, 10092, 10697, 12671, and 21339 processed with the `CIAO` toolkit (version 4.15; Fruscione et al. 2006).

We then retrieve the H.E.S.S. >2 TeV image described in H.E.S.S. Collaboration et al. (2018) with improved angular and spectral resolution. Finally, we also use data from the Mopra southern Galactic plane CO survey data release 3 (Braiding et al. 2018) in order to trace the distribution of the molecular gas clouds associated with RX J1713. We produce maps of the $J = 1 - 0$ transitions of ^{12}CO with 0.′6 spatial resolution and 0.1 km s^{-1} velocity resolution integrated in the −6 to −16 km s^{-1} velocity range, associated with the distance to RX J1713 (Fukui et al. 2003; Cassam-Chenaï et al. 2004) using the `CARTA` software (Comrie et al. 2021).

3. Results

3.1. Polarization Maps

The IXPE telescopes have an angular resolution (half-power diameter) of ∼30″, allowing us to produce spatially resolved maps of the X-ray polarization properties. In Figure 2 (left), we show the polarization map of the northwest rim of RX J1713 obtained by using the `PMAPCUBE` algorithm, binned with a pixel size of 2′ (that is, about four IXPE point-spread functions), with the vectors indicating the direction of the magnetic field, orthogonal to the observed PA. Binned maps require a trade-off in determining the pixel size: if this is too small, there will not be enough statistics to achieve a significant

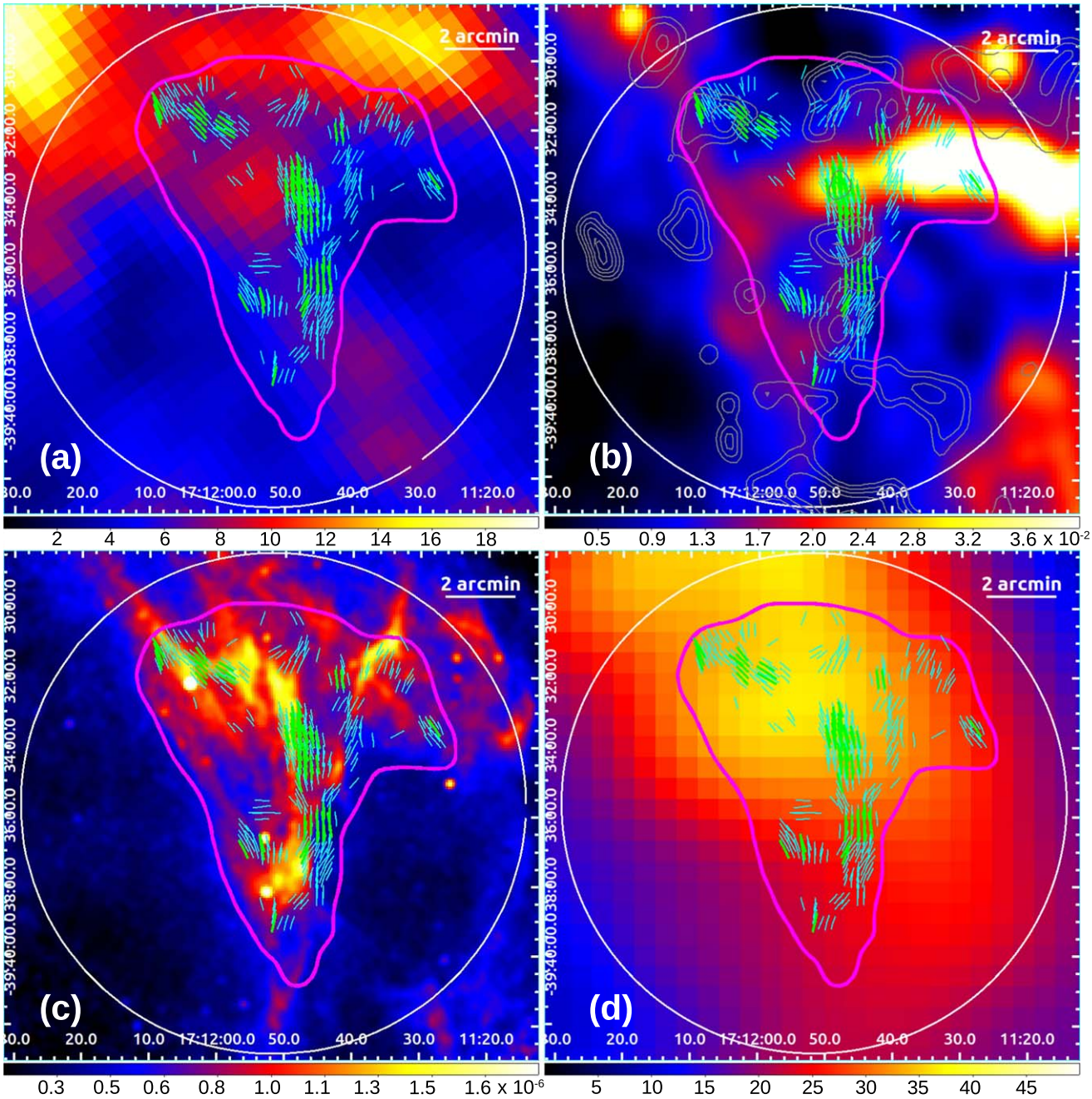

Figure 3. (a) Mopra ^{12}CO image of RX J1713 integrated in the -6 to -16 km^{-1} velocity range. (b) ATCA 20 cm image of the northwest region of RX J1713; the gray contours are the radio polarization levels, with each level corresponding to a 2% PD increase. (c) Chandra exposure-corrected mosaic of 0.5−7 keV images of the northwest of RX J1713. (d) H.E.S.S. >2 TeV excess count map of the northwest of RX J1713. In all panels, we show the IXPE field of view as a white circle, the IXPE 2−5 keV contours in magenta, and the P1, P2, and P3 regions as solid white ellipses. In cyan and green, we show the magnetic field lines obtained through Gaussian smoothing of the IXPE data with $>2\sigma$ and $>3\sigma$, respectively.

measurement, and if too big, the polarization may be diluted. For this reason, we also applied a smoothing technique to the polarization maps with an oversampled pixel size of 10.″5, and we increased the signal-to-noise ratio by smoothing the images with a Gaussian kernel of 6 pixels (corresponding to about $\sim 1'$). We show this smoothed map in Figure 2 (right). In both maps, the significance of the magnetic field directions is color-coded as $>2\sigma$ in cyan and $>3\sigma$ in green. In the binned map, we find 4 pixels with significance higher than 3σ. In the smoothed map, instead, we identify three elliptical regions of high significance that we call P1, P2, and P3 and are broadly consistent with the positions of the most significant pixels in the binned map.

Figure 3(a) shows the Mopra ^{12}CO image of RX J1713 integrated in the -6 to -16 km^{-1} velocity range overlapped by the magnetic field inferred from the IXPE observation. The other panels of Figure 3 show the ATCA 20 cm radio image (b), the high-resolution broadband Chandra image (c), and the H.E.S.S. >2 TeV excess counts image (d). In the radio image, we also show the radio PD as gray contours of 2% steps. In the ^{12}CO image, the high-significance polarization is measured in regions that appear to have lower gas density, while in the

20 cm radio image, there is a weak correlation between radio emission/polarization and X-ray polarization. On the other hand, the IXPE results overlaid on the high-resolution Chandra image show the magnetic field lines following the shape of the curvature of the shock. Because of the low spatial resolution of the H.E.S.S. γ-ray image, no new information can be derived at the present time.

3.2. Model-independent Polarization Results

For each region of interest, we show the observed PD and PA as polar plots in Figure 4, with their 50%, 90%, 99%, and 99.9% confidence level contours, obtained from the PCUBE analysis. Their values are tabulated in Table 1 together with the values calculated after background subtraction. The polarization signal from the region "All" (made from the combination of regions N, S, and W shown in the right panel of Figure 1) is detected at a significance of 5.2σ, with an average PD of $13.0\% \pm 3.5\%$, after background subtraction. In the combined N and S subregions of the shell, we have a detection at 4.8σ with a PD of $12.8\% \pm 3.7\%$, after background subtraction. Individually, we detect X-ray polarization in the N and S parts of the shell at 3.7σ and 4.0σ, respectively, with an intrinsic PD of $12.4\% \pm 4.2\%$ and $18.3\% \pm 5.3\%$. In each region, we find the PAs to be consistent with being orthogonal to the shock direction. We do not obtain statistically significant detection for the W part of the shell. The three smaller regions, P1, P2, and P3, selected from the polarization maps show significant (3.9σ, 5.6σ, and 4.8σ) PDs of $25.2\% \pm 8.0\%$, $45.1\% \pm 8.3\%$, and $46.0\% \pm 9.8\%$, after background subtraction, that are higher than the average shell value and, with PAs again consistent with being perpendicular to the local shock, in agreement with those of the entire shell.

In contrast to what was previously done in other IXPE observations of SNRs (e.g., in Vink et al. 2022; Ferrazzoli et al. 2023), and similarly to the results obtained on SN 1006 (Zhou et al. 2023), in RX J1713, a realignment of the Stokes parameters according to a radial or tangential magnetic field model, using the xpstokesalign tool, yields no conclusive evidence of a circular symmetry over a uniform distribution. This is because of the large angular size of the remnant and the difficulty in determining the reference frame center for the Stokes parameter realignment. Hence, we test the hypothesis of a constant magnetic field direction in the region encompassing the P1, P2, and P3 regions using the test statistic,

$$\chi^2 = \sum_{n=1}^{3} \frac{(\mathrm{PA}n - \mathrm{PA}_w)^2}{\mathrm{PA}n_{\mathrm{ERR}}^2}, \quad (1)$$

where the weighted mean PA_w is 105° and PAn and PAn_{ERR}, with n from 1 to 3, are the measured PAs and their uncertainties for the regions P1, P2, and P3, respectively. The estimated test-statistic value is $\chi^2 = 29.9$ with 2 degrees of freedom. Thus, the probability that the PA is constant is only 3.26×10^{-7}. The major axes of the elliptical regions, P1, P2, and P3, on the right panel in Figure 1 follow the bright arc in the IXPE count map that in turn is along the shock front. These major axes are normal to the directions of PA in the P1, P2, and P3 regions, respectively, within statistical errors. This suggests that the magnetic field is tangential to the shock front.

3.3. Spectropolarimetric Analysis

A model-dependent approach for calculating the polarization of the five regions is to use the I, Q, and U spectra. First, we extracted source and background spectra from the previously defined regions. For each region, we then jointly fit the background-subtracted I, Q, and U spectra with a model obtained by combining foreground absorption, power-law spectrum, and PD and PA constant in the 2−5 keV energy band (*tbabs* ∗ *powerlaw* ∗ *constpol*) in XSPEC. We fixed N_{H} in the IXPE spectropolarimetric analysis to 8.15×10^{21} cm^{-2} based on Tsuji et al. (2021) and left the power-law index, normalization, and polarization values as free parameters. The results of the fit are tabulated in Table 1 and show agreement with the model-independent results for both the PD and PA. Also, the best-fit value of the photon spectral index Γ is in agreement with the values of ∼2.0−2.4 for the region observed by IXPE as reported in the literature (Koyama et al. 1997; Slane et al. 1999; Uchiyama et al. 2003; Cassam-Chenaï et al. 2004; Lazendic et al. 2004; Hiraga et al. 2005; Sano et al. 2015; Tsuji et al. 2019). In Figure 5, we present the spectropolarimetric fit for the "All" region as an example.

4. Discussion

4.1. Behavior of the Magnetic Field

The discovery of a tangential magnetic field in RX J1713 differs from previous IXPE findings that revealed radial magnetic fields for other young SNRs, Cas A, Tycho, and SN 1006 (Vink et al. 2022; Ferrazzoli et al. 2023; Zhou et al. 2023). In these three cases, it was argued that hydrodynamical instabilities responsible for the onset of the radial field at longer wavelengths appear to be already active at subparsec scales, close to particle acceleration sites.

The tangential magnetic field in RX J1713 is instead compatible with a model of anisotropic turbulence produced by the shock compression of an upstream isotropic turbulence (Bykov et al. 2020). In this model, as the turbulence is swept across the shock upon compression, the magnetic field becomes predominantly tangential to the shock front, resulting in predominantly radial synchrotron polarization. Interestingly, as suggested by the polarization map and the Chandra X-ray image (Figure 3(c)), the highest PDs we reported are very close to the shock front, with offsets from the peak polarization up to 1′. There may be shifts between IXPE and Chandra—due to proper motions and/or alignment issues—but based on the measured expansion rate (Tsuji & Uchiyama 2016), the shock would have shifted by 8″ at most over the 10 yr baseline, much less than the IXPE angular resolution. Moreover, we found no misalignment between the IXPE and Chandra images. So, if IXPE itself shows that the X-ray emission peak is not cospatial with the polarization peak, this could imply that the turbulence level of the magnetic field is increasing further downstream of the shock.

Under our interpretation, the PD is determined by the ratio of chaotic-to-ordered magnetic fields in the X-ray-emitting regions. The PD values are observed to differ considerably between the four SNRs studied to date, and differences in the ambient conditions may play a role. However, the distinctly different magnetic field geometry inferred for RX J1713, which reminds one of the already-known dichotomy observed in the radio band, suggests fundamental differences in the development of the ordered field component, making it difficult to draw firm

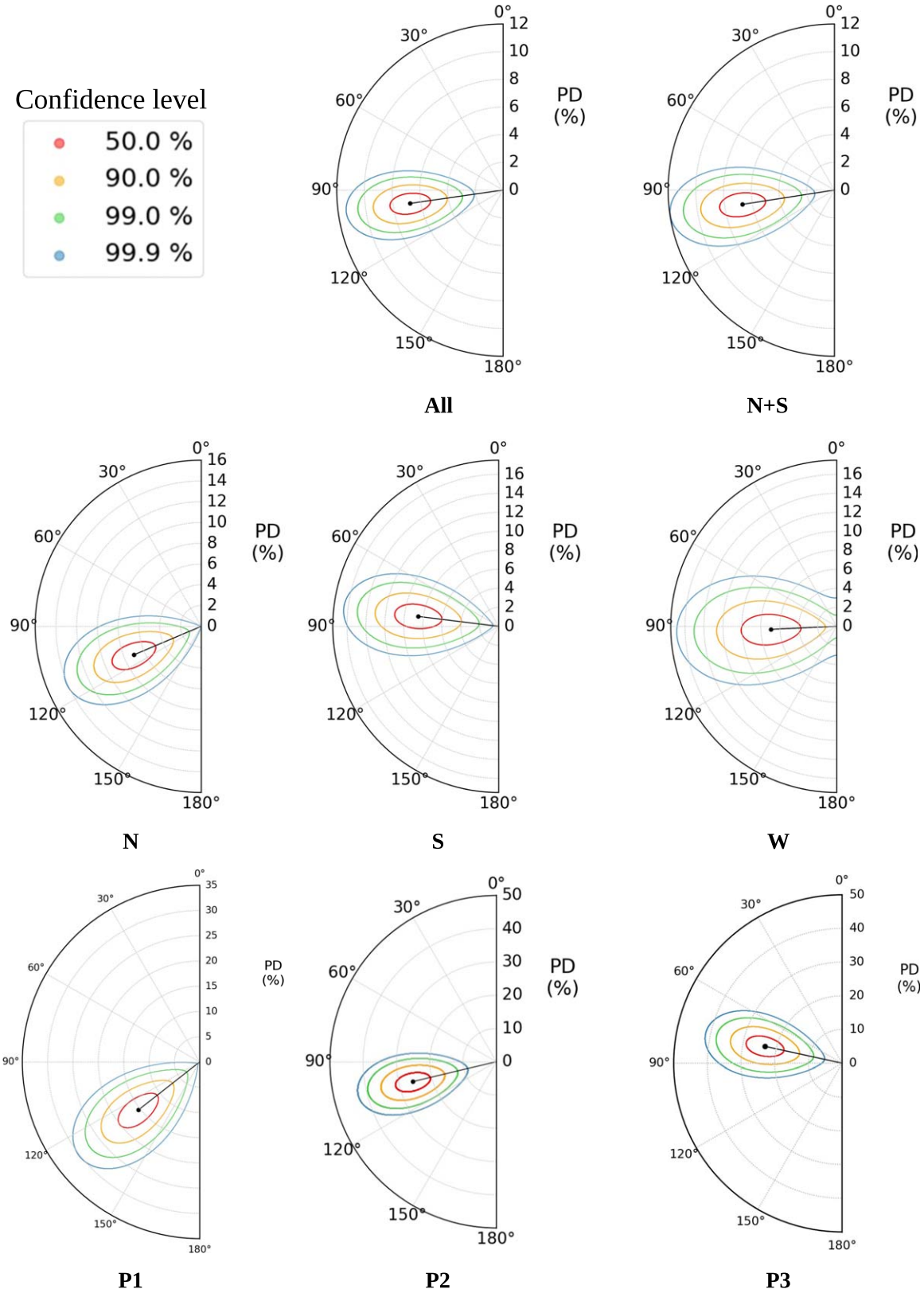

Figure 4. Polarization plots by region of interest obtained with PCUBE in the 2−5 keV energy band. In each polar plot, we show the observed PD and PA in radial and position angle coordinates, respectively. The black dots mark the measured PD and PA values. We represent the 50%, 90%, 99%, and 99.9% confidence levels (based upon χ^2 with 2 degrees of freedom) as red, orange, green, and blue contours, respectively.

conclusions on the chaotic magnetic field component. The reason for the dichotomy is not fully understood, because it involves so many aspects of SNR physics—magnetic field amplification due to CR acceleration, instability at the shock front dependent on ambient conditions, instability within the SNR shell due to its internal structure, and, ultimately, SN

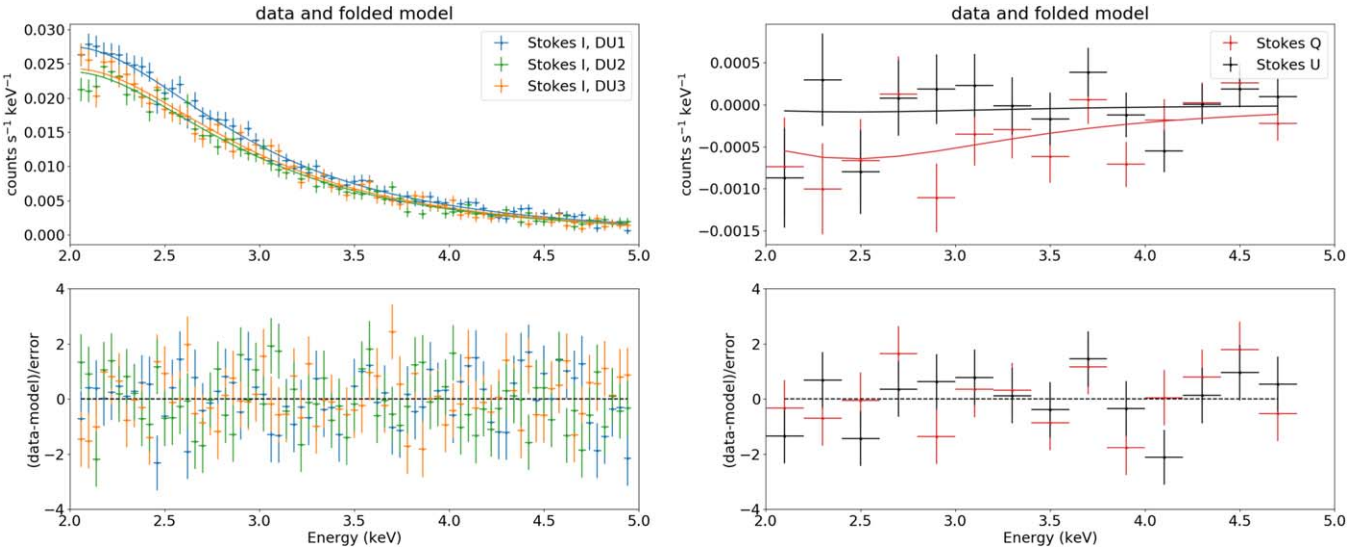

Figure 5. Spectropolarimetric fit of the Stokes *I*, *Q*, and *U* spectra of the region "All" (data points) and the best-fit model (solid lines). In the bottom panels, we show the residuals in terms of (data-model)/error. The Stokes *I* spectra from the three DU observations are coded using different colors and shown in the left panels. The Stokes *Q* and *U* spectra are grouped for ease of visualization and shown in the right panels. Note that the normalization among the three DUs is known to fluctuate at low energies, but this does not affect the goodness of the fit.

Table 1
Polarization Results for the IXPE Regions of Interest with PCUBE and XSPEC and ATCA Radio Observations

	IXPE PCUBE						IXPE XSPEC				Radio
Shell Region	PD_{obs} (%)	PA_{obs} (deg)	PD (%)	PA (deg)	σ	CL (%)	PD (%)	PA (deg)	Γ	χ/d.o.f.	PD_{radio} (%)
All	6.8 ± 1.3	98.2 ± 5.3	13.0 ± 3.5	95.8 ± 7.7	5.2	99.999	12.0 ± 3.1	93.7 ± 7.4	2.11 ± 0.04	1.10	4.5 ± 1.7
N + S	6.7 ± 1.4	98.9 ± 6.1	12.8 ± 3.7	96.5 ± 8.3	4.8	99.998	12.5 ± 3.3	96.7 ± 7.6	2.04 ± 0.04	1.02	4.8 ± 1.4
N	7.0 ± 1.9	113.0 ± 7.7	12.4 ± 4.2	111.7 ± 9.7	3.7	99.897	12.3 ± 3.8	114.0 ± 8.9	2.10 ± 0.04	0.99	4.8 ± 1.8
S	8.5 ± 2.1	83.0 ± 7.1	18.3 ± 5.3	80.8 ± 8.3	4.0	99.968	19.3 ± 4.7	79.0 ± 7.1	2.21 ± 0.05	0.91	4.8 ± 0.9
W	<13.8	ND	<29.7	ND	2.6	96.519	<25.6	ND	2.04 ± 0.06	1.22	3.2 ± 1.6
P1	15.4 ± 4.0	128.2 ± 7.4	26.5 ± 7.4	128.2 ± 8.0	3.9	99.941	25.2 ± 6.7	135.3 ± 7.6	2.16 ± 0.08	0.93	5.6 ± 1.1
P2	25.9 ± 4.6	103.4 ± 5.1	45.1 ± 8.3	103.0 ± 5.3	5.7	99.999	35.6 ± 7.6	103.8 ± 6.1	2.21 ± 0.08	0.90	3.5 ± 1.4
P3	23.4 ± 4.9	77.7 ± 5.9	46.0 ± 9.8	77.0 ± 6.1	4.8	99.999	36.9 ± 9.1	76.0 ± 7.0	2.23 ± 0.10	1.03	5.2 ± 0.9

Note. In the PD_{obs} and PA_{obs} columns are the observed values, while the ones in the PD and PA columns for both the IXPE PCUBE and IXPE XSPEC tables are the values after background subtraction. The radio PDs from Lazendic et al. (2004) are the average polarization values in a given region plus/minus the standard deviation.

explosion dynamics—that no simple description can be taken as fully reliable. The general idea is that the dichotomy is due to the presence or absence of RT instability at the CD separating the SN ejecta from the shocked interstellar matter (ISM). This strongly depends on the acceleration to which the SNR shell is subject, and this is stronger in younger remnants than in older ones (where young versus old is not just a matter of age but of the expansion regime). So it is likely that RT instability is more efficient in stretching the magnetic field in the radial direction in younger systems than in older ones. It is unlikely that X-ray-emitting particles are volume filling and hence subject to the effect of RT instability at the CD. The action of RM instability at the very shock front—which previous papers (Vink et al. 2022; Ferrazzoli et al. 2023; Zhou et al. 2023) attributed the radial magnetic field to—might also have some dependence of the dynamics of the SNR, making younger (and hence faster) systems more prone to it (but also on ISM conditions, in particular the presence of density gradients). The magnetic field structure in the upstream could also be reshaped by the efficiency of CR acceleration. Unfortunately, with just four SNRs reported by IXPE so far, it is hard to find any reasonable and robust trend. To make any meaningful attribution, we would need a better characterization of these SNRs. For these reasons, we defer in-depth discussions on comparisons between the different SNRs to a future publication.

4.2. Magnetic Field Turbulence

While the exact nature of both ordered and turbulent components of the magnetic field still remains uncertain, we can place constraints on their relative magnitudes through the observed PD. Here we use the Bandiera & Petruk (2016) model to describe the connection between observed PD, photon spectral index Γ, and turbulence level of the magnetic field $\delta B/B_0$ of a source.

This model assumes that a uniform field B_0 is superposed on the random field of the source. The random component has a Gaussian distribution—with a kernel of δ_B—isotropic on average, so that the stronger the random magnetic field component, the smaller the PD. We find that for the "All" region of RX J1713, $\delta B/B_0 = 1.6 \pm 0.2$, while for the P1, P2, and P3 regions, it is

1.0 ± 0.2, 0.6 ± 0.1, and 0.6 ± 0.2, respectively. The shock-compressed model of Bandiera & Petruk (2016), where $\delta B_{\rm tan} = 4\sqrt{2}\,\delta B_{\rm perp}$,[56] gives an expected downstream PD of ∼69% with tangential direction for an RX J1713 average photon spectral index of 2.2 and isotropic upstream magnetic turbulence. There are two options to obtain the IXPE maximum measured value of PD $\simeq$ 40%. One is to assume that in the upstream, there is a net radial magnetic field. In this case, using an extension of the model of Bandiera & Petruk (Bandiera & Petruk 2024), one needs $B_{\rm perp}/\delta B \simeq 1.4-1.5$ in the upstream, implying $\delta B/B_0 < 1$, contrary to spectral model fitting and to expectations from acceleration theory. The other option is to assume that here we see mainly the effect of shock compression, whereas further downstream of the shock, as suggested by the comparison with the Chandra image in Figure 3(c), the turbulence has partially reisotropized (maybe due to other instabilities acting to stretch the radial component). In this case, in order to reduce the PD to the measured values, a lower level of anisotropy with $\delta B_{\rm tan} \sim 2.5\delta B_{\rm perp}$ is required.

As an explanation of the different turbulence levels among the SNRs seen by IXPE, Zhou et al. (2023) put forward properties of the environment, in particular the ambient density. Indeed, the remnant with the smallest detected PD, Cas A, is evolving in a medium with an average density of $0.9 \pm 0.3\,{\rm cm}^{-3}$ (Lee et al. 2014). In the RX J1713 case, the intercloud density is instead $\sim 0.01-0.1$ cm^{-3} (Cassam-Chenaï et al. 2004; Katsuda et al. 2015; Tsuji & Uchiyama 2016). SN 1006, which has a maximum PD comparable with that of RX J1713, is also in a rarefied environment with density $\sim 0.05-0.085$ cm^{-3} (Acero et al. 2007; Giuffrida et al. 2022). Therefore, our findings support the suggestion that high PD peaks are achieved in the presence of low ambient density. The ambient density also affects the maximum size of the Bell instability for the most rapid growth mode. According to Bell (2004), upstream turbulent magnetic fields can be generated by nonresonant streaming instability driven by CR current. We can deduce that this kind of instability is acting in RX J1713 because it can grow if $\delta B >> B_0$, a condition possible only in the presence of an isotropic turbulence upstream. Since the shock compression enhances only tangential components, every isotropic turbulence upstream becomes mainly tangential downstream. The length scale of the Bell instability is given by Bell (2004):

$$\lambda_{\rm Bell} \sim 1.4 \times 10^{18}\,{\rm cm}\left(\frac{V_{\rm s}}{3900\ {\rm km\ s^{-1}}}\right)^{-3} \left(\frac{n_0}{0.015\ {\rm cm^{-3}}}\right)^{-1}\left(\frac{E_{\rm max}}{100\ {\rm TeV}}\right)\left(\frac{B_0}{3\ \mu{\rm G}}\right), \quad (2)$$

where $V_{\rm s}$ is the shock velocity (value of ∼3900 km s^{-1} taken from Tsuji et al. 2021), n_0 is the ambient density (value of 0.015 cm^{-3} from Tsuji & Uchiyama 2016), $E_{\rm max}$ is the maximum energy, and B_0 is the unshocked magnetic field. At a distance of 1 kpc, this $\lambda_{\rm Bell}$ value corresponds to ∼90″, equivalent to 3 times the IXPE angular resolution and similar in size to the regions P1, P2, and P3. Because the smallest regions for which we detect significant polarization are comparable in scale with the Bell (2004) wavelength, we cannot claim that we see the effect of the streaming instability in the turbulence and a consequent effect on the orientation of the magnetic field.

[56] Here $B_{\rm tan}$ and $B_{\rm perp}$ are defined as the magnetic field components tangential and perpendicular to the shock, respectively.

4.3. Bohm Factor and Age

The IXPE observation of RX J1713 also allows us to test two scenarios linking polarization with other source features: (1) the closer the Bohm factor, η, is to unity, the lower the PD; and (2) younger SNRs have lower PD (shocks are faster and magnetic fields are more turbulent), whereas older remnants tend to have higher PD. The Bohm factor is defined as the ratio of the mean free path of the particle diffusion to the particle gyroradius, and it is connected to magnetic field turbulence in the quasi-linear region as

$$\eta = \left(\frac{B_0}{\delta B}\right)^2, \quad (3)$$

with B_0 the initial background magnetic field and δB the turbulent field. The observed cutoff energy in the X-ray synchrotron emission, ϵ_0, corresponds to maximum particle energy in the acceleration region, which in turn is connected to the Bohm factor and shock speed $v_{\rm sh}$ (Tsuji et al. 2021):

$$\eta = 1.6\left(\frac{v_{\rm sh}}{4000\ {\rm km\ s^{-1}}}\right)^2\left(\frac{\epsilon_0}{\rm keV}\right)^{-1}. \quad (4)$$

Measurements of the cutoff energy and shock speed can thus provide estimates of the Bohm factor. The closer the Bohm factor is to unity, the more turbulent the B field on subparsec scales is, and the lower the polarization would be. RX J1713 is recognized as an accelerator operating at the most efficient rate —i.e., the acceleration proceeds in a regime close to the Bohm limit of $\eta \simeq 1$ (Tanaka et al. 2008; Tsuji et al. 2019)—indeed, Tsuji et al. (2021) estimate for this source $\eta = 1.4 \pm 0.3$. Even with a Bohm factor close to unity, RX J1713 can achieve the observed PD only if the magnetic field is tangential to the shock front (e.g., Casse et al. 2001), as CR electrons can spread near the shock in an anisotropic way, with a much slower diffusion across than along the magnetic field lines.

The second scenario is also a possibility, as age estimates of RX J1713 (possibly associated with SNR 393) make it the oldest SNR observed by IXPE to date.

4.4. Comparison with Other Wavelengths

4.4.1. Comparison with Radio Data

In Figure 3(b), we show the RX J1713 ATCA 20 cm image —with a ∼70″ beam size—centered on the IXPE field of view with the magnetic field direction inferred by X-ray polarimetry and radio polarization measured by Lazendic et al. (2004) shown as overlays. Lazendic et al. (2004) detected significant linear polarization of 3%−7% toward the western shell of RX J1713 in the region observed by IXPE, at 1.4 GHz and 2.4 GHz. The large Faraday rotation measure, RM > 100 rad m^{-2} (e.g., Lazendic et al. 2004), severely affects the PA at radio frequencies and limits polarization measurements to patches of the brightest radio filaments. Consequently, they were unable to determine the intrinsic orientation of the magnetic field from available data. In contrast, polarization in the X-ray regime does not suffer from Faraday rotation. For this reason, the IXPE observation represents the first instance in which it has been possible to map the magnetic field in the

northwest region of RX J1713. As shown in Table 1, the X-ray PD in the considered regions is larger than the ∼5% radio value, as expected for the steeper X-ray index (∼2.2) with respect to the radio index (∼1.5), which allows for higher maximum PD (∼69% in the radio, ∼77% in the X-ray), and by the smaller volume sampled by the X-ray emission that is less prone to depolarization effects due to different magnetic field orientations along the line of sight (Vink & Zhou 2018). In a recent publication by Cotton et al. (2024), based on MeerKAT data, the radio polarization of the SNRs G4.8+6.2 and G7.7–3.7 raises potential questions pertaining to an age dependence on the magnetic field morphology. Both remnants show evidence for tangential magnetic fields similar to what we infer from IXPE measurements of RX J1713. X-ray observations of G7.7–3.7 (Zhou et al. 2018) indicate a relatively young age for the remnant based on the density and ionization timescale of the plasma. Based on these estimates and the sky position of the remnant, these authors suggest a possible association with SN 386. The remnant G4.8+6.2 is significantly above the Galactic plane, and it could be a very high-energy γ-ray source corresponding to a 4σ hot spot in the H.E.S.S. significance map (H.E.S.S. Collaboration et al. 2022). Suggestions of a young age and possible association with the year 1163 CE Korean "guest star" have been made (Liu et al. 2019). However, the estimated distance—which is highly uncertain—yields either an uncomfortably large remnant or a surprisingly low radio luminosity for such an interpretation. If the remnant is indeed associated with an event from 1163 CE, the tangential fields are in stark contrast to the radial fields observed for SN 1006 based on IXPE measurements. Finally, the 1738 yr old SNR 1E 0102.2–7219 in the Small Magellanic Cloud was found with ATCA to have a tangential magnetic field (Alsaberi et al. 2024). Therefore, there may be emerging evidence that the radial magnetic fields observed in the youngest SNRs give way to tangential magnetic fields in remnants with ages of only 1000–2000 yr.

4.4.2. Comparison with γ-ray Data

The IXPE X-ray polarimetry of RX J1713 also provides new input for the debate on the leptonic versus hadronic nature of its γ-ray emission. In Figure 3(d), we show the magnetic field direction inferred by X-ray polarimetry superimposed on the H.E.S.S. >2 TeV image (H.E.S.S. Collaboration et al. 2018) of the IXPE field of view. The substantial coincidence of X-ray and γ-ray emission favors a leptonic origin of the latter (Aharonian et al. 2006; H.E.S.S. Collaboration et al. 2018): the same electron population could be the source of both synchrotron and likely inverse-Compton emission. In Figure 3(a), we show the ^{12}CO distribution compared to the magnetic field direction inferred by IXPE. Indeed, there are some ^{12}CO molecular clouds in the range of –6 to –16 km s^{-1} associated with RX J1713 (Sano et al. 2013), with a large uncertainty in their position along the line of sight, but the compressed magnetic field appears to be in correspondence with lower-density regions. The hadronic scenario generally invokes dense clumps as the origin of the γ-ray emission (Gabici & Aharonian 2014; Fukui et al. 2021). However, if radial magnetic fields are indeed caused by RM instabilities triggered in a clumpy medium (Inoue et al. 2013), then the tangential magnetic field in RX J1713 suggests that the medium in which RX J1713 evolves is a much less clumpy environment than in those young SNRs for which radial magnetic fields have been reported. This includes the environment of the high-Galactic-latitude SN 1006. This argument is not incontrovertible, but the IXPE results on RX J1713 narrow down the possibilities for explaining either radial magnetic fields in young SNRs or the hadronic γ-ray scenario for RX J1713. Given the interest in the theoretical explanation of the nature of the γ-ray emission from RX J1713, it would be useful, in the future, to look with IXPE at the other RX J1713 regions to compare magnetic field direction in different regions with a different surrounding medium, in particular, the northern spot—where there is less X-ray flux with respect to the γ one—or the southwest, which mostly resembles the northwest region observed by IXPE.

5. Conclusions

We reported on the IXPE observation of the northwestern part of the SNR RX J1713 for ∼830 ks in the 2−5 keV energy band. We performed a spatially resolved search for polarization using both model-dependent and model-independent techniques. Our analysis shows that the polarization direction is normal to the shock and that the average PD in the whole region is $12.5\% \pm 3.3\%$. These results are consistent with a model of shock compression of an upstream isotropic turbulence producing a predominantly tangential magnetic field. The other remnants observed by IXPE—Cas A, Tycho, and the northeast limb of SN 1006—all showed radial magnetic fields, making RX J1713 the first example with shock-compressed magnetic fields. A deeper analysis of the nature of this important difference will be carried out in a future work.

We estimated the magnetic field turbulence level based on the observed PD and photon spectral index. Our results suggest that either there is a net radial magnetic field in the upstream region or the turbulence partially reisotropized downstream. The latter requires a lower level of anisotropy to justify the PD measured in this remnant. We discussed two scenarios: (1) the closer the Bohm factor η to unity—as in RX J1713—the lower the PD, and (2) younger SNRs have lower PD than older remnants. For the first scenario, the observed PD can be achieved only if the magnetic field is perpendicular to the shock normal, even with $\eta \sim 1$. As for the second scenario, the possible association of RX J1713 with SNR 393 suggests that it is the oldest SNR observed by IXPE, which may also influence its polarization characteristics. The maximum PD detected, $41.5\% \pm 9.5\%$, and the low ambient density, $\sim 0.01-0.1$ cm^{-3}, in which RX J1713 is evolving also support the hypothesis that magnetic turbulence, and hence particle acceleration in SNRs, is environment-dependent.

We compared the results in the X-ray band and other wavelengths and found that the average X-ray PD is higher than the 3%−7% one measured by ATCA in the radio band at 20 cm in the same regions. Because of the large uncertainties in the determination of radio PA, the magnetic field morphology had been unknown. This IXPE measurement thus represents the first map of the magnetic field lines in RX J1713. Future radio polarimetric observation of RX J1713 with, for example, MeerKAT would allow one to compare the X-ray and radio morphology of the magnetic field.

X-ray polarimetry of RX J1713 also provides new input for the debate on the leptonic versus hadronic nature of its γ-ray emission, supporting the former scenario. If radial magnetic fields are caused by RM instabilities triggered in a clumpy medium—which is generally required by the hadronic scenario for the γ-ray emission—then the observed tangential magnetic

field suggests that RX J1713 evolves in an environment where the hadronic γ-ray scenario is less favored.

The upcoming IXPE observations of relatively co-aged SNRs such as RCW 86 and Vela Jr. will further shed light on the complex panorama that spatially resolved X-ray polarimetry is unveiling and allow for a systematic study of their polarimetric properties.

Acknowledgments

The Imaging X-ray Polarimetry Explorer (IXPE) is a joint US and Italian mission. The US contribution is supported by the National Aeronautics and Space Administration (NASA) and led and managed by its Marshall Space Flight Center (MSFC), with industry partner Ball Aerospace (contract NNM15AA18C). The Italian contribution is supported by the Italian Space Agency (Agenzia Spaziale Italiana, ASI) through contract ASI-OHBI-2022-13-I.0, agreements ASI-INAF-2022-19-HH.0 and ASI-INFN-2017.13-H0, and its Space Science Data Center (SSDC) with agreements ASI-INAF-2022-14-HH.0 and ASI-INFN 2021-43-HH.0 and by the Istituto Nazionale di Astrofisica (INAF) and the Istituto Nazionale di Fisica Nucleare (INFN) in Italy. This research used data products provided by the IXPE Team (MSFC, SSDC, INAF, and INFN) and distributed with additional software tools by the High-Energy Astrophysics Science Archive Research Center (HEASARC) at NASA Goddard Space Flight Center (GSFC). E.Co., A.D.M., R.F., P.So., S.F., F.L.M., and F. Mu. are partially supported by MAECI with grant CN24GR08 "GRBAXP: Guangxi-Rome Bilateral Agreement for X-ray Polarimetry in Astrophysics." C.-Y.N. is supported by a GRF grant of the Hong Kong Government under HKU 17305419. This Letter employs a list of Chandra data sets, obtained by the Chandra X-ray Observatory, contained in DOI:10.25574/cdc.240. We thank Tony Bell, Rino Bandiera, and Damiano Caprioli for the helpful discussions.

Facilities: IXPE, CXO, ATCA, HESS, Mopra

Software: `CARTA` (Comrie et al. 2021), `CIAO` (Fruscione et al. 2006), `ixpeobssim` (Baldini et al. 2022), `XSPEC` (Arnaud 1996).

Appendix
Background Treatment

A.1. Galactic X-Ray Background

Because RX J1713 is located on the Galactic plane, the Galactic ridge X-ray background (GRXB; see, e.g., Ebisawa et al. 2005) may not be negligible. In order to estimate its value, we extract the spectrum from a Chandra observation (ObsID 10091) of RX J1713 in a region on a chip outside of the remnant. Then, we subtract the spectrum of the associated blank sky and fit it with an APEC model with electron temperature (kT) fixed at 8 keV, following Katsuda et al. (2015) and Tsuji et al. (2019). The estimated 2−5 keV GRXB flux is $\sim 5.9 \pm 0.3 \times 10^{-13}$ erg cm^{-2} s^{-1}, about 15 times smaller than the $\sim 9.161 \pm 0.002 \times 10^{-12}$ erg cm^{-2} s^{-1} source flux from the "All" region.

A.2. IXPE Rejected Instrumental Background

We selected the two local background regions, called East and West (as shown in Figure 1), so as to satisfy the following criteria:

1. encompassing regions with a surface brightness of $\leqslant 0.45$ counts arcsec^{-2},
2. no farther than 6′ from center in order to not be contaminated by spurious edge effects, and
3. at least 45″ (i.e., about 1.5 times the IXPE angular resolution) from the "All" region in order to avoid contamination from the source polarization.

Table 2
Stokes Parameters and Surface Area of the Background Regions in the 2−5 keV Energy Band

Region	Surface arcmin^2	Q/I (%)	U/I (%)
Background East	19.72	1.20 ± 2.90	-2.50 ± 2.90
Background West	9.71	-3.34 ± 4.00	1.25 ± 4.00
Background East + West	29.43	-0.34 ± 2.36	-1.22 ± 2.36

As shown in Table 2, both the individual background regions and the combined East + West background are found to be unpolarized, with the most stringent limit being PD < 7.3% at a 99% confidence level in the 2−5 keV energy band for the East + West background. The intrinsic PD can be obtained by subtracting the `PCUBE` of the background—after scaling it for the ratio of the region size—from the `PCUBE` of the region of interest, thanks to the additive properties of the Stokes parameters, and the uncertainties on the Stokes parameters are linearly propagated to the polarimetric observables according to Kislat et al. (2015).

We also perform a spectropolarimetric study of the background, extracting the I, Q, and U spectra from the background regions East and West. We fit the spectra with a model comprising three components. The first is the GRXB; we model this component as an absorbed (*Tbabs* with nH = 8.15×10^{21} cm^{-2}) *apec* with temperature kT = 8 keV (Katsuda et al. 2015; Tsuji et al. 2019). The second component is an absorbed power law describing the residual SNR emission; we fit this emission using spectra of the same background region on Chandra data (ObsID 6370) and find the index (∼2.2) and relative flux (1.67×10^{-12} erg cm^{-2} s^{-1} versus 1.24×10^{-12} erg cm^{-2} s^{-1} in the 2−5 keV energy band, respectively) with respect to the aforementioned CRXB emission. The third, and more conspicuous, component is the unrejected IXPE instrumental background that we model empirically with an unabsorbed broken power law. We fix the indexes to 2.3 and −0.378 and the energy break at 3.08 keV by simultaneously fitting the spectra of the background field of ∼1.5 Ms worth of publicly available IXPE observations of high-Galactic-latitude blazars and other extragalactic point sources: PSR B0540–69 (ObsID 02001299), PG 1553+113 (02004999), IC 4329A (01003601), and 1ES 0229+200 (01006499).

We show the spectropolarimetric fit of the RX J1713 background region in Figure 6. As it was found by studying the background region in a model-independent way, no significant polarization is measured for each component. The statistical significance of the fit is given by $\chi^2 = 296.66$ with 287 degrees of freedom. By comparing the background-subtracted Stokes I spectrum for the "All" region and the model of the background spectrum, the background flux becomes comparable to or brighter than the source flux above ∼5 keV, as shown in Figure 7. For this reason, we select only the 2−5 keV energy band to study the polarization properties.

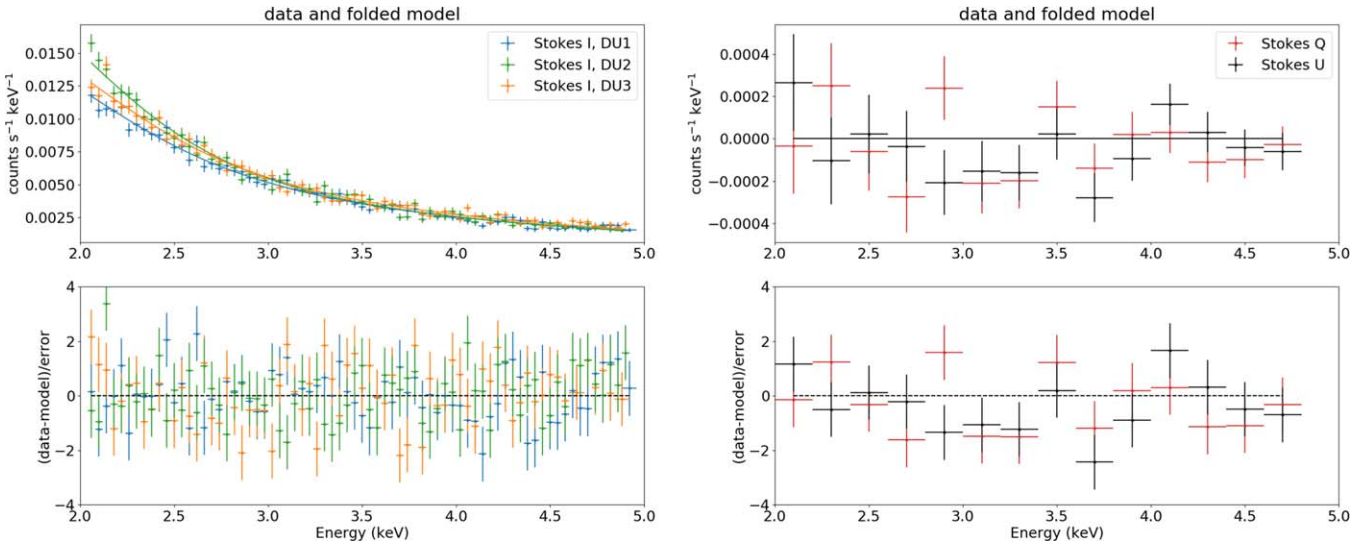

Figure 6. Spectropolarimetric fit of the Stokes *I*, *Q*, and *U* spectra of the background region (data points) and the best-fit model (solid lines). In the bottom panels, we show the residuals in terms of (data-model)/error. The Stokes *I* spectra from the three DU observations are coded using different colors and shown in the left panels. The Stokes *Q* and *U* spectra are instead grouped for ease of visualization and shown in the right panels.

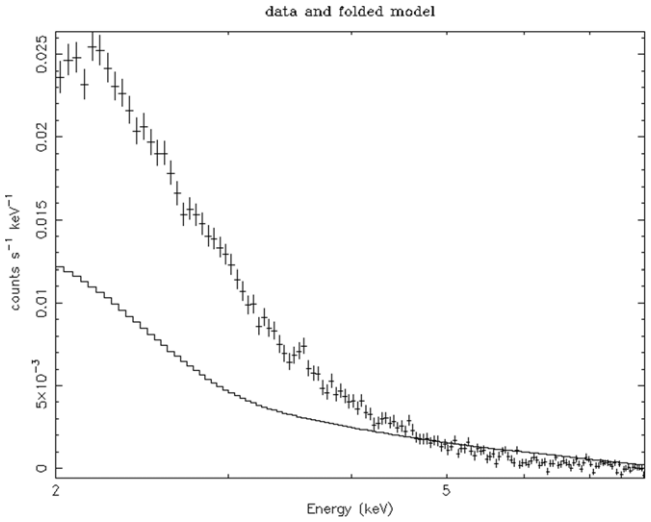

Figure 7. Background-subtracted spectra for the region "All" of the shell for the three DUs (data points) compared with the best-fit model of the background (solid line).

ORCID iDs

Riccardo Ferrazzoli https://orcid.org/0000-0003-1074-8605
Niccolò Bucciantini https://orcid.org/0000-0002-8848-1392
Patrick Slane https://orcid.org/0000-0002-6986-6756
Jacco Vink https://orcid.org/0000-0002-4708-4219
Martina Cardillo https://orcid.org/0000-0001-8877-3996
Yi-Jung Yang https://orcid.org/0000-0001-9108-573X
Stefano Silvestri https://orcid.org/0000-0002-8665-0105
Ping Zhou https://orcid.org/0000-0002-5683-822X
Enrico Costa https://orcid.org/0000-0003-4925-8523
Nicola Omodei https://orcid.org/0000-0002-5448-7577
C.-Y. Ng https://orcid.org/0000-0002-5847-2612
Paolo Soffitta https://orcid.org/0000-0002-7781-4104
Martin C. Weisskopf https://orcid.org/0000-0002-5270-4240
Luca Baldini https://orcid.org/0000-0002-9785-7726
Alessandro Di Marco https://orcid.org/0000-0003-0331-3259
Victor Doroshenko https://orcid.org/0000-0001-8162-1105
Jeremy Heyl https://orcid.org/0000-0001-9739-367X
Philip Kaaret https://orcid.org/0000-0002-3638-0637
Dawoon E. Kim https://orcid.org/0000-0001-5717-3736
Frédéric Marin https://orcid.org/0000-0003-4952-0835
Tsunefumi Mizuno https://orcid.org/0000-0001-7263-0296
Melissa Pesce-Rollins https://orcid.org/0000-0003-1790-8018
Carmelo Sgrò https://orcid.org/0000-0001-5676-6214
Douglas A. Swartz https://orcid.org/0000-0002-2954-4461
Toru Tamagawa https://orcid.org/0000-0002-8801-6263
Fei Xie https://orcid.org/0000-0002-0105-5826
Iván Agudo https://orcid.org/0000-0002-3777-6182
Lucio A. Antonelli https://orcid.org/0000-0002-5037-9034
Matteo Bachetti https://orcid.org/0000-0002-4576-9337
Wayne H. Baumgartner https://orcid.org/0000-0002-5106-0463
Ronaldo Bellazzini https://orcid.org/0000-0002-2469-7063
Stefano Bianchi https://orcid.org/0000-0002-4622-4240
Stephen D. Bongiorno https://orcid.org/0000-0002-0901-2097
Raffaella Bonino https://orcid.org/0000-0002-4264-1215
Alessandro Brez https://orcid.org/0000-0002-9460-1821
Fiamma Capitanio https://orcid.org/0000-0002-6384-3027
Simone Castellano https://orcid.org/0000-0003-1111-4292
Elisabetta Cavazzuti https://orcid.org/0000-0001-7150-9638
Chien-Ting Chen https://orcid.org/0000-0002-4945-5079
Stefano Ciprini https://orcid.org/0000-0002-0712-2479
Alessandra De Rosa https://orcid.org/0000-0001-5668-6863
Ettore Del Monte https://orcid.org/0000-0002-3013-6334
Laura Di Gesu https://orcid.org/0000-0002-5614-5028
Niccolò Di Lalla https://orcid.org/0000-0002-7574-1298
Immacolata Donnarumma https://orcid.org/0000-0002-4700-4549
Michal Dovčiak https://orcid.org/0000-0003-0079-1239

Steven R. Ehlert https://orcid.org/0000-0003-4420-2838
Teruaki Enoto https://orcid.org/0000-0003-1244-3100
Yuri Evangelista https://orcid.org/0000-0001-6096-6710
Sergio Fabiani https://orcid.org/0000-0003-1533-0283
Javier A. Garcia https://orcid.org/0000-0003-3828-2448
Shuichi Gunji https://orcid.org/0000-0002-5881-2445
Wataru Iwakiri https://orcid.org/0000-0002-0207-9010
Svetlana G. Jorstad https://orcid.org/0000-0001-6158-1708
Vladimir Karas https://orcid.org/0000-0002-5760-0459
Fabian Kislat https://orcid.org/0000-0001-7477-0380
Jeffery J. Kolodziejczak https://orcid.org/0000-0002-0110-6136
Henric Krawczynski https://orcid.org/0000-0002-1084-6507
Fabio La Monaca https://orcid.org/0000-0001-8916-4156
Luca Latronico https://orcid.org/0000-0002-0984-1856
Ioannis Liodakis https://orcid.org/0000-0001-9200-4006
Simone Maldera https://orcid.org/0000-0002-0698-4421
Alberto Manfreda https://orcid.org/0000-0002-0998-4953
Andrea Marinucci https://orcid.org/0000-0002-2055-4946
Alan P. Marscher https://orcid.org/0000-0001-7396-3332
Herman L. Marshall https://orcid.org/0000-0002-6492-1293
Francesco Massaro https://orcid.org/0000-0002-1704-9850
Giorgio Matt https://orcid.org/0000-0002-2152-0916
Fabio Muleri https://orcid.org/0000-0003-3331-3794
Michela Negro https://orcid.org/0000-0002-6548-5622
Stephen L. O'Dell https://orcid.org/0000-0002-1868-8056
Chiara Oppedisano https://orcid.org/0000-0001-6194-4601
Alessandro Papitto https://orcid.org/0000-0001-6289-7413
George G. Pavlov https://orcid.org/0000-0002-7481-5259
Abel L. Peirson https://orcid.org/0000-0001-6292-1911
Matteo Perri https://orcid.org/0000-0003-3613-4409
Pierre-Olivier Petrucci https://orcid.org/0000-0001-6061-3480
Maura Pilia https://orcid.org/0000-0001-7397-8091
Andrea Possenti https://orcid.org/0000-0001-5902-3731
Juri Poutanen https://orcid.org/0000-0002-0983-0049
Simonetta Puccetti https://orcid.org/0000-0002-2734-7835
Brian D. Ramsey https://orcid.org/0000-0003-1548-1524
John Rankin https://orcid.org/0000-0002-9774-0560
Ajay Ratheesh https://orcid.org/0000-0003-0411-4243
Oliver J. Roberts https://orcid.org/0000-0002-7150-9061
Roger W. Romani https://orcid.org/0000-0001-6711-3286
Gloria Spandre https://orcid.org/0000-0003-0802-3453
Fabrizio Tavecchio https://orcid.org/0000-0003-0256-0995
Roberto Taverna https://orcid.org/0000-0002-1768-618X
Allyn F. Tennant https://orcid.org/0000-0002-9443-6774
Nicholas E. Thomas https://orcid.org/0000-0003-0411-4606
Francesco Tombesi https://orcid.org/0000-0002-6562-8654
Alessio Trois https://orcid.org/0000-0002-3180-6002
Sergey S. Tsygankov https://orcid.org/0000-0002-9679-0793
Roberto Turolla https://orcid.org/0000-0003-3977-8760
Kinwah Wu https://orcid.org/0000-0002-7568-8765
Silvia Zane https://orcid.org/0000-0001-5326-880X

References

Abdo, A. A., Ackermann, M., Ajello, M., et al. 2011, ApJ, 734, 28
Acero, F., Ballet, J., & Decourchelle, A. 2007, A&A, 475, 883
Acero, F., Ballet, J., Decourchelle, A., et al. 2009, A&A, 505, 157
Acero, F., Katsuda, S., Ballet, J., & Petre, R. 2017, A&A, 597, A106
Ackermann, M., Ajello, M., Allafort, A., et al. 2013, Sci, 339, 807
Aharonian, F., Akhperjanian, A. G., Bazer-Bachi, A. R., et al. 2006, A&A, 449, 223
Aharonian, F., Akhperjanian, A. G., Bazer-Bachi, A. R., et al. 2007, A&A, 464, 235
Aharonian, F. A., Akhperjanian, A. G., Aye, K. M., et al. 2004, Natur, 432, 75
Alsaberi, R. Z. E., Filipović, M. D., Dai, S., et al. 2024, MNRAS, 527, 1444
Amato, E. 2014, IJMPD, 23, 1430013
Arnaud, K. A. 1996, in ASP Conf. Ser. 101, Astronomical Data Analysis Software and Systems V, ed. G. H. Jacoby & J. Barnes (San Francisco, CA: ASP), 17
Baldini, L., Barbanera, M., Bellazzini, R., et al. 2021, APh, 133, 102628
Baldini, L., Bucciantini, N., Lalla, N. D., et al. 2022, SoftX, 19, 101194
Bandiera, R., & Petruk, O. 2016, MNRAS, 459, 178
Bandiera, R., & Petruk, O. 2024, arXiv:2405.14534
Bell, A. R. 2004, MNRAS, 353, 550
Bellazzini, R., Angelini, F., Baldini, L., et al. 2006, NIMPA, 560, 425
Braiding, C., Wong, G. F., Maxted, N. I., et al. 2018, PASA, 35, e029
Bucciantini, N., Di Lalla, N., Romani, R. W. R., et al. 2023, A&A, 672, A66
Bykov, A. M., Uvarov, Y. A., Slane, P., & Ellison, D. C. 2020, ApJ, 899, 142
Cassam-Chenaï, G., Decourchelle, A., Ballet, J., et al. 2004, A&A, 427, 199
Casse, F., Lemoine, M., & Pelletier, G. 2001, PhRvD, 65, 023002
Celli, S., Morlino, G., Gabici, S., & Aharonian, F. A. 2019, MNRAS, 490, 4317
Comrie, A., Wang, K.-S., Hsu, S.-C., et al. 2021, CARTA: The Cube Analysis and Rendering Tool for Astronomy, v2.0.0, Zenodo, doi: 10.5281/zenodo.3377984
Costa, E., Soffitta, P., Bellazzini, R., et al. 2001, Natur, 411, 662
Cotton, W., Kothes, R., Camilo, F., et al. 2024, ApJS, 270, 21
Cristofari, P. 2021, Univ, 7, 324
Di Marco, A., Costa, E., Muleri, F., et al. 2022, AJ, 163, 170
Di Marco, A., Soffitta, P., Costa, E., et al. 2023, AJ, 165, 143
Dickel, J. R., & Jones, E. M. 1990, in IAU Symp. 140, Galactic and Intergalactic Magnetic Fields, ed. R. Beck, P. P. Kronberg, & R. Wielebinski (Dordrecht: Kluwer), 81
Ebisawa, K., Tsujimoto, M., Paizis, A., et al. 2005, ApJ, 635, 214
Ellison, D. C., Patnaude, D. J., Slane, P., & Raymond, J. 2010, ApJ, 712, 287
Ellison, D. C., Slane, P., Patnaude, D. J., & Bykov, A. M. 2012, ApJ, 744, 39
Federici, S., Pohl, M., Telezhinsky, I., Wilhelm, A., & Dwarkadas, V. V. 2015, A&A, 577, A12
Ferrazzoli, R., Slane, P., Prokhorov, D., et al. 2023, ApJ, 945, 52
Finke, J. D., & Dermer, C. D. 2012, ApJ, 751, 65
Fruscione, A., McDowell, J. C., Allen, G. E., et al. 2006, Proc. SPIE, 6270, 62701V
Fukui, Y., Moriguchi, Y., Tamura, K., et al. 2003, PASJ, 55, L61
Fukui, Y., Sano, H., Sato, J., et al. 2012, ApJ, 746, 82
Fukui, Y., Sano, H., Yamane, Y., et al. 2021, ApJ, 915, 84
Fürst, E., & Reich, W. 2004, in The Magnetized Interstellar Medium, ed. B. Uyaniker, W. Reich, & R. Wielebinski (Göttingen: Copernicus), 141
Gabici, S., & Aharonian, F. A. 2014, MNRAS, 445, L70
Ginzburg, V. L., & Syrovatskii, S. I. 1964, The Origin of Cosmic Rays (New York: Macmillan)
Ginzburg, V. L., & Syrovatskii, S. I. 1965, ARA&A, 3, 297
Giuffrida, R., Miceli, M., Caprioli, D., et al. 2022, NatCo, 13, 5098
Gull, S. F. 1973, MNRAS, 162, 135
H.E.S.S. Collaboration, Abdalla, H., Abramowski, A., et al. 2018, A&A, 612, A6
H. E. S. S. Collaboration, Aharonian, F., Ait Benkhali, F., et al. 2022, A&A, 662, A65
Hiraga, J. S., Uchiyama, Y., Takahashi, T., & Aharonian, F. A. 2005, A&A, 431, 953
Inoue, T., Shimoda, J., Ohira, Y., & Yamazaki, R. 2013, ApJL, 772, L20
Jones, T. J., Rudnick, L., DeLaney, T., & Bowden, J. 2003, ApJ, 587, 227
Jun, B.-I., & Norman, M. L. 1996, ApJ, 472, 245
Katsuda, S., Acero, F., Tominaga, N., et al. 2015, ApJ, 814, 29
Kislat, F., Clark, B., Beilicke, M., & Krawczynski, H. 2015, APh, 68, 45
Koyama, K., Kinugasa, K., Matsuzaki, K., et al. 1997, PASJ, 49, L7
Koyama, K., et al. 1995, Natur, 378, 255
Lazendic, J. S., Slane, P. O., Gaensler, B. M., et al. 2004, ApJ, 602, 271
Lee, J.-J., Park, S., Hughes, J. P., & Slane, P. O. 2014, ApJ, 789, 7
Liu, Y., Zou, Y.-C., Jiang, B., et al. 2019, MNRAS, 490, L21
Malkov, M. A., & Drury, L. O. 2001, RPPh, 64, 429
Milne, D. K., & Dickel, J. R. 1975, AuJPh, 28, 209
Pfeffermann, E., & Aschenbach, B. 1996, in Roentgenstrahlung from the Universe, ed. H. U. Zimmermann, J. Trümper, & H. Yorke, 267
Sano, H., Fukuda, T., Yoshiike, S., et al. 2015, ApJ, 799, 175

Sano, H., Tanaka, T., Torii, K., et al. 2013, ApJ, 778, 59
Slane, P., Gaensler, B. M., Dame, T. M., et al. 1999, ApJ, 525, 357
Soffitta, P., Baldini, L., Bellazzini, R., et al. 2021, AJ, 162, 208
Tanaka, T., Uchiyama, Y., Aharonian, F. A., et al. 2008, ApJ, 685, 988
Tsuji, N., & Uchiyama, Y. 2016, PASJ, 68, 108
Tsuji, N., Uchiyama, Y., Aharonian, F., et al. 2019, ApJ, 877, 96
Tsuji, N., Uchiyama, Y., Khangulyan, D., & Aharonian, F. 2021, ApJ, 907, 117
Uchiyama, Y., Aharonian, F. A., & Takahashi, T. 2003, A&A, 400, 567
van der Laan, H. 1962, MNRAS, 124, 125
Vink, J., Prokhorov, D., Ferrazzoli, R., et al. 2022, ApJ, 938, 40
Vink, J., & Zhou, P. 2018, Galax, 6, 46
Wang, Z. R., Qu, Q. Y., & Chen, Y. 1997, A&A, 318, L59
Weisskopf, M. C., Soffitta, P., Baldini, L., et al. 2022, JATIS, 8, 026002
West, J. L., Jaffe, T., Ferrand, G., Safi-Harb, S., & Gaensler, B. M. 2017, ApJL, 849, L22
Zhou, P., Prokhorov, D., Ferrazzoli, R., et al. 2023, ApJ, 957, 55
Zhou, P., Vink, J., Li, G., & Domček, V. 2018, ApJL, 865, L6